Evidence for quantum spin liquid behavior in single-layer 1T-$TaSe_2$ from scanning tunneling microscopy

Wei Ruan[1,2,†], Yi Chen[1,2,†], Shujie Tang[3,4,5,6,7], Jinwoong Hwang[5,8], Hsin-Zon Tsai[1,10], Ryan L. Lee[1], Meng Wu[1,2], Hyejin Ryu[5,9], Salman Kahn[1], Franklin Liou[1], Caihong Jia[1,2,11], Andrew Aikawa[1], Choongyu Hwang[8], Feng Wang[1,2,12], Yongseong Choi[13], Steven G. Louie[1,2], Patrick A. Lee[14], Zhi-Xun Shen[3,4], Sung-Kwan Mo[5], Michael F. Crommie[1,2,12,*]

[1]*Department of Physics, University of California, Berkeley, California 94720, USA*

[2]*Materials Sciences Division, Lawrence Berkeley National Laboratory, Berkeley, California 94720, USA*

[3]*Stanford Institute for Materials and Energy Sciences, SLAC National Accelerator Laboratory and Stanford University, Menlo Park, California 94025, USA*

[4]*Geballe Laboratory for Advanced Materials, Departments of Physics and Applied Physics, Stanford University, Stanford, California 94305, USA*

[5]*Advanced Light Source, Lawrence Berkeley National Laboratory, Berkeley, California 94720, USA*

[6]*CAS Center for Excellence in Superconducting Electronics, Shanghai Institute of Microsystem and Information Technology, Chinese Academy of Sciences, Shanghai 200050, China*

[7]*School of Physical Science and Technology, Shanghai Tech University, Shanghai 200031, China*

[8]*Department of Physics, Pusan National University, Busan 46241, Korea*

[9]*Center for Spintronics, Korea Institute of Science and Technology, Seoul 02792, Korea*

[10]*International Collaborative Laboratory of 2D Materials for Optoelectronic Science & Technology of Ministry of Education, Engineering Technology Research Center for 2D Material Information Function Devices and Systems of Guangdong Province, Shenzhen University, Shenzhen 518060, China*

[11]*Henan Key Laboratory of Photovoltaic Materials and Laboratory of Low-dimensional Materials Science, School of Physics and Electronics, Henan University, Kaifeng 475004, China*

[12]*Kavli Energy Nano Sciences Institute at the University of California Berkeley and the Lawrence Berkeley National Laboratory, Berkeley, California 94720, USA*

[13]*Advanced Photon Source, Argonne National Laboratory, Argonne, Illinois 60439, USA*

[14]*Department of Physics, Massachusetts Institute of Technology, Cambridge MA 02139, USA*

† These authors contributed equally to this work.

**e-mail: crommie@berkeley.edu*

Abstract

Two-dimensional triangular-lattice antiferromagnets are predicted under some conditions to exhibit a quantum spin liquid ground state with no energy barrier to creating emergent, fractionalized spinon excitations that carry spin but no charge. Materials that realize this kind of spin liquid are expected to have low-energy behavior described by a spinon Fermi surface. Directly imaging the resulting spinons, however, is difficult due to their chargeless nature. Here we use scanning tunneling spectroscopy to image density waves consistent with predictions of spinon density modulation arising from a spinon Fermi surface instability in single-layer 1T-$TaSe_2$. We confirm the existence of a triangular lattice of localized spins in this material by contacting it to a metallic 1H-$TaSe_2$ substrate and measuring the Kondo effect. Spectroscopic imaging of isolated single-layer 1T-$TaSe_2$ reveals long-wavelength super-modulations at Hubbard band energies, consistent with the predicted behavior of itinerant spinons. These super-modulations allow direct experimental measurement of the spinon Fermi wavevector, in good agreement with theoretical predictions for a two-dimensional quantum spin liquid.

Since the first predictions by Anderson in 1973[1], quantum spin liquids (QSLs) have been intensely investigated[2-7] as candidates to host exotic quantum phenomena such as fractionalized elementary excitations[2-4], topological order[4,5], and unconventional superconductivity[6,7]. QSLs are a novel state of matter predicted to arise in quantum antiferromagnets where geometric frustration and quantum fluctuations are strong enough to prevent a magnetically ordered ground state[2-4]. A key to understanding the QSL state is its low-energy physics, often dominated by emergent fractional fermions (termed spinons) that carry spin-1/2 but no charge[2-4]. Many QSL models are based on two-dimensional (2D) triangular-lattice Mott insulators[2-4], and several material candidates incorporating coupled 2D layers have been found to exhibit behavior consistent with spinon excitations[8-10]. It remains debatable whether the spinons in such systems are gapped or not[4,8-10], but increasing evidence[10] suggests the existence of gapless spinons that exhibit a Fermi surface[2-4,8-13].

Imaging the itinerant spinons, however, is challenging due to their fractional and chargeless nature. Some predictions suggest that the spinon Fermi surface should host instabilities leading to spinon spatial patterns[13] that can, in principle, be imaged by single-particle scanned probes[14]. Bulk 1T-TaS_2 has been suggested as one such QSL candidate[15-21]. This layered material is believed to exhibit a Mott insulator ground state that arises cooperatively from a star-of-David charge density wave (CDW)[22-24]. Each star-of-David cluster contributes one localized spin, thus forming a triangular spin lattice. Some evidence for QSL behavior in bulk 1T-TaS_2 has been found, such as the absence of magnetic order down to millikelvin temperature[17-19] and a linear term in the thermal conductivity[20,21], but QSL physics here is complicated by interlayer coupling. This is because interlayer coupling can lead to spin delocalization and/or interlayer spin-singlet formation, which are detrimental to forming a gapless QSL state[15,19,25-27].

Here we report experimental evidence supporting the existence of a QSL-based spinon Fermi surface in single-layer (SL) 1T-$TaSe_2$ through the use of scanning tunneling microscopy/spectroscopy (STM/STS). SL 1T-$TaSe_2$ is a newly discovered 2D Mott insulator that exhibits a low-temperature star-of-David CDW phase similar to bulk 1T-TaS_2 (i.e., the star-of-David cells are centered at Ta atoms - Supplementary Fig. 1), but which does not suffer from the disadvantages of interlayer coupling between 1T layers[28,29]. We report two experimental findings that support the presence of a QSL in SL 1T-$TaSe_2$. First we demonstrate the existence of localized spins on a triangular lattice in SL 1T-$TaSe_2$ through the observation of a Kondo resonance at the Fermi level (E_F) when SL 1T-$TaSe_2$ is placed in contact with metallic 1H-$TaSe_2$. Next we show evidence for a QSL-based spinon Fermi surface subject to a Fermi surface instability in isolated SL 1T-$TaSe_2$ through the observation of long-wavelength super-modulations in the electronic local density of states (LDOS) at the Hubbard band energies. Such wave patterns are unexpected in an insulator but occur naturally in the presence of a spinon Fermi surface. The ability to access fractional spinon behavior via a single-particle probe (i.e., STM) arises from the decomposition of injected electrons into spinons (chargeless spin-1/2 fractional particles) and chargons (spinless charged fractional particles)[14,30]. By imaging spinon-induced LDOS super-modulations we are able to directly determine the spinon Fermi wavevector (k_F), in good agreement with theoretical predictions[15,16] for a 2D QSL.

Kondo resonance in a 1T/1H $TaSe_2$ vertical heterostructure

SL $TaSe_2$ films were grown on epitaxial bilayer graphene (BLG) terminated 6H-SiC(0001) substrates and also on cleaved graphite surfaces via molecular beam epitaxy (MBE)[29,31]. A single layer of $TaSe_2$ contains one Ta atomic layer sandwiched between a pair of Se atomic layers, with each Ta atom coordinated by six Se atoms (Fig. 1a). The Se cage forms an octahedron in the metastable 1T-phase and a trigonal prism in the stable 1H-phase. Coexisting 1T and 1H phases were grown via MBE in the SL limit under controlled growth conditions, as shown by our STM images (Fig. 1b). Atomically-flat 1T and 1H SL islands can easily be distinguished as seen by close-up images of both phases in the insets to Fig. 1b which exhibit a triangular $\sqrt{13} \times \sqrt{13}$ star-of-David CDW pattern for the 1T-phase[29] and a 3 × 3 CDW pattern for the 1H-phase[31]. Vertical heterostructures composed of a single 1T layer on top of a single 1H layer (1T/1H) are observed to display the star-of-David CDW pattern in the top layer and the 3 × 3 CDW in the bottom layer (Fig. 1b and Supplementary Fig. 2b).

We verified the electronic structure of the different $TaSe_2$ phases by measuring STM differential conductance (dI/dV) (which reflects surface electronic LDOS) as a function of sample bias voltage (V_b). dI/dV spectra acquired on metallic SL 1H-$TaSe_2$ islands show finite LDOS at E_F accompanied by a slight suppression due to CDW formation (Fig. 2a green curves), consistent with previous measurements[31]. dI/dV spectra acquired on insulating SL 1T-$TaSe_2$ islands on BLG/SiC, on the other hand, show a Mott gap (Fig. 2a red curves), also consistent with previous measurements[29]. Here the LDOS peak near V_b = -0.3 V is identified as the lower Hubbard band (LHB) and the upper Hubbard band (UHB) corresponds to the peaks near V_b = 0.2 V (UHB_1) and V_b = 0.6 V (UHB_2) (these are split due to reduced screening in 2D[29]). The electronic structure of both SL 1T and 1H phases was also identified using angle-resolved photoemission spectroscopy (ARPES) (Supplementary Fig. 3b), confirming the coexistence of both phases.

dI/dV spectra acquired on 1T/1H vertical heterostructures are very different from either of the bare SL spectra at the Hubbard band energy scale. The heterostructure spectra reveal a pronounced zero bias peak (ZBP) that is absent from single layers (Fig. 2a blue curves) and which cannot be explained by doping[32-35] or strain (Supplementary Note 2.1). The ZBP was found to persist in every star-of-David cell (Supplementary Fig. 2). We identify the ZBP as a Kondo resonance[36,37], which is expected to arise when a local spin (from the 1T layer) couples to itinerant electrons in a metal (from the 1H layer)[38] (the absence of a Kondo resonance for SL 1T-$TaSe_2$ on BLG is due to BLG's low carrier density and poor coupling to the 1T layer (Supplementary Note 2.2)). To test the Kondo hypothesis we examined the ZBP feature over the temperature range 5 K $\leqslant T \leqslant$ 70 K, as plotted in Fig. 2b. The ZBP gradually broadens with increased temperature by an amount that cannot be accounted for by pure thermal broadening, but is well-fit by a thermally-convolved Fano line shape (Supplementary Note 2.3 and Supplementary Fig. 2d, e) with an intrinsic temperature-dependent width $\Gamma(T)$. The intrinsic resonance width as a function of temperature (T) is observed to follow the well-known Kondo expression[37]

$$\Gamma(T) = \sqrt{(\pi k_B T)^2 + 2(k_B T_K)^2} \#(1)$$

where k_B is the Boltzmann constant, yielding an estimated Kondo temperature of $T_K = 57 \pm 3$ K (Fig. 2c, red dashed line) and a resultant Kondo-coupling of $J_K \approx 0.2$ eV (Supplementary Note 2.4). The observation of the Kondo resonance peak in every star-of-David CDW cell suggests the existence of localized spins in isolated SL 1T-$TaSe_2$ that are arranged in a triangular lattice (Fig. 1c) (this behavior is consistent with the typical lateral extension of Kondo peaks (which is on the order of 1 nm[39]), as well as with the coherence temperature of the 1T/1H Kondo lattice being lower than the STM base temperature of 5 K (Supplementary Note 2.4)). Measuring magnetism in single-layer materials via more direct methods is challenging. For example, we attempted to probe magnetism in SL 1T-$TaSe_2$ using X-ray magnetic circular dichroism but this yielded no observable magnetization beyond the noise level (Supplementary Fig. 4).

Super-modulations in single-layer 1T-$TaSe_2$

We explored possible QSL behavior in isolated single layers of 1T-$TaSe_2$ (i.e., that are supported by BLG/SiC rather than the metallic 1H-$TaSe_2$ phase) by characterizing long-wavelength super-modulations in the real-space electronic structure of this triangular spin lattice (the Kondo effect plays no significant role for this material combination

(Supplementary Note 2.2)). Measurements were performed on SL 1T-$TaSe_2$ islands like the one shown in Fig. 3a which exhibit dI/dV spectra characteristic of a Mott insulator (Fig. 3b). Fig. 3c-g shows constant-height dI/dV maps acquired at different energies in the area outlined by a yellow dashed square in Fig. 3a, while Fig. 3h-l reveals the corresponding Fourier transform (FT) of each dI/dV map (see Supplementary Fig. 5 for FT images without labels). The star-of-David CDW pattern dominates the empty-state LDOS for energies above the UHB[29] as seen by the dI/dV map at $V_b = 1.0$ V in Fig. 3c and its FT in Fig. 3h. Here the CDW triangular lattice yields 6-fold symmetric FT peaks marked by red circles and labeled as the primary reciprocal lattice vectors $\mathbf{b}_i$ ($1 \leqslant i \leqslant 6$). These define the first Brillouin zone of the star-of-David CDW (red hexagon). No other periodicities are seen at this energy.

New longer-wavelength super-modulations emerge at lower energies closer to the Hubbard band energies (i.e., UHB_2, UHB_1, and LHB). At energies near UHB_2 ($V_b = 0.62$ V), for example, a new super-modulation is clearly seen in the real-space image of Fig. 3d as bright patches of enhanced LDOS (see also Supplementary Fig. 6d). This structure corresponds to a triangular grid rotated by 30° from the CDW lattice with an incommensurate lattice constant slightly larger than $\sqrt{3}a$ (Supplementary Fig. 6) where a is the CDW lattice constant. This incommensurate super-modulation (ICS) is best seen in Fig. 3i (the FT of Fig. 3d) which shows new peaks marked by blue circles along the Γ-K directions inside the CDW Brillouin zone. The ICS wavevector, $\mathbf{q}_{\mathrm{ICS}}$, can be written in terms of the CDW reciprocal lattice vectors as $\mathbf{q}_{\mathrm{ICS}} = q_{\mathrm{ICS}}(\mathbf{b}_1 + \mathbf{b}_2)$ where $q_{\mathrm{ICS}} = 0.241 \pm 0.009$ (q_{ICS} is obtained from Gaussian fits of FTs acquired on 10 different islands with 5 different tips - Supplementary Fig. 7).

The ICS pattern is also observed when energy is lowered further to UHB_1, as seen by the dI/dV map at $V_b = 0.2$ V (Fig. 3e) and corresponding FT (Fig. 3j). The ICS is often obscured in real space images due to mixing with the CDW pattern (Supplementary Note 1), but its FT peaks are easily resolved from the CDW wavevectors (Fig. 3j). The ICS persists as energy is lowered to the LHB as seen in the dI/dV map at V_b = -0.18 V (Fig. 3f) which yields FT peaks at $\mathbf{q}_{\mathrm{ICS}}$ (Fig. 3k). The filled-state LHB measurement, however, differs from the empty-state UHB measurements in that it also exhibits a short-range commensurate super-modulation (CS) of wavelength $\sqrt{3}a$ that yields broad FT peaks at the K-points of the CDW Brillouin zone (green circles in Fig. 3k - see also Supplementary Fig. 8). Both the ICS and CS disappear at energies below the LHB where only the star-of-David CDW remains as shown by the dI/dV map at V_b = -0.8 V (Fig. 3g) and its corresponding FT (Fig. 3l).

The complete energy dependence of the super-modulations over the energy range -1V < V_b < 1.5 V is shown in Fig. 4a and b (Supplementary Figs. 9 and 10 show additional data at selected energies). Here the energy-dependent FT amplitude along the Γ-K direction (black dashed line in the inset to Fig. 4a) as a function of wavevector $\mathbf{q} = q(\mathbf{b}_1 + \mathbf{b}_2)$ shows three main features: (i) the CDW reciprocal lattice vector $\mathbf{b}_1 + \mathbf{b}_2$ ($q = 1$) over a wide energy range (black dashed ovals), (ii) the CS ($q = 1/3$) in the filled-state LHB (green dashed oval), and (iii) the ICS ($q = q_{\mathrm{ICS}} \approx 1/4$) in both the LHB and UHB regimes (blue dashed ovals). We observe that the ICS wavevector is independent of energy, but its *amplitude* is not. To better visualize the energy dependence of the ICS amplitude, its strength is defined as the ICS FT peak amplitude $\rho(E, \mathbf{q}_{\mathrm{ICS}})$ normalized by the FT peak amplitude $\rho(E, \mathbf{q} = \mathbf{0})$ (equivalent to the spatially averaged surface LDOS). Fig. 4b shows that this ratio, $|\rho(E, \mathbf{q}_{\mathrm{ICS}})/\rho(E, \mathbf{q} = \mathbf{0})|$ (blue dots), is small at all energies except for the LHB and UHB regimes (a SL 1T-$TaSe_2$ dI/dV spectrum is plotted for reference (black line)). The temperature dependence of the ICS amplitude (Supplementary Fig. 11) shows that it decreases as temperature is raised and completely vanishes by T = 77 K, whereas the star-of-David CDW remains even up to room temperature.

In order to investigate possible substrate effects on the behavior of the observed super-modulation, SL 1T-$TaSe_2$ was also grown on cleaved graphite (HOPG) via MBE and characterized by STM/STS. These samples also exhibit star-of-David CDW order and Mott insulating behavior similar to films grown on BLG/SiC as shown by the STM images and d*I*/d*V* spectra of Supplementary Fig. 12. STM images acquired in the LHB of SL 1T-$TaSe_2$/HOPG and their FTs show the same ICS pattern as seen for SL 1T-$TaSe_2$/BLG/SiC (Supplementary Fig. 12d and e). However, an additional 2 × 2 super-modulation (with respect to the CDW lattice) is sometimes seen for SL 1T-$TaSe_2$/HOPG in the LHB that has FT peaks near the M points (Fig. 5d and Supplementary Fig. 12f-k) (this was seen for 2 out of 11 islands). We refer to this new super-modulation wavevector as $\mathbf{q}_{\mathrm{M}}$. $\mathbf{q}_{\mathrm{ICS}}$ and $\mathbf{q}_{\mathrm{M}}$ were never simultaneously observed on the same SL 1T-$TaSe_2$/HOPG island.

Relationship between super-modulations and QSL behavior

Our experimental results support the hypothesis that SL 1T-$TaSe_2$ is a 2D QSL. The first piece of evidence is that SL 1T-$TaSe_2$ contains a triangular lattice of localized spins, an essential ingredient for a QSL. This evidence is provided by our observation of the Kondo effect in 1T-layers supported by a 1H-layer, which implies that each star-of-David in isolated SL 1T-$TaSe_2$ contains a single quantum spin (such Kondo screening does not occur when 1T-layers are supported by graphene (Supplementary Note 2.2)). The second piece of evidence is the long-wavelength super-modulations that we observe in SL 1T-$TaSe_2$ (when it is supported by graphene) via STS imaging. These periodicities lie at the precise energies and wavevectors expected for a QSL, as discussed below.

Before describing how these super-modulations are explained by QSL considerations, however, we first rule out possible alternative explanations. The first alternative possibility is electronic quasiparticle interference (QPI). Our observed ICS pattern is inconsistent with QPI because its wavelength is energy independent over the Hubbard bandwidths. There are also no significant electronic structure features at the Hubbard band edges that might induce a QPI signal at $\mathbf{q}_{ICS}$ (Supplementary Fig. 13). The second alternative possibility is a structural distortion such as a moiré pattern and/or a surface reconstruction. This explanation is unlikely because the observed super-modulations exist only over very specific energy ranges involving the Hubbard bands, suggesting that they are electronic and/or spin-based phenomena. To further exclude moiré patterns involving complex BLG/SiC reconstructions we point to the fact that SL 1T-$TaSe_2$/HOPG exhibits the same ICS modulation as SL 1T-$TaSe_2$/BLG/SiC (Supplementary Fig. 12). This is significant because HOPG has no reconstruction and cannot combine with 1T-$TaSe_2$ to yield an ICS moiré pattern. We additionally see no evidence of the super-modulation in low-energy electron diffraction (LEED) patterns[29], and no evidence that it is a strain effect (Supplementary Note 3.1). Reconstruction of the star-of-David CDW (i.e., subharmonic phonon softening) is also unlikely since the star-of-David CDW is accounted for by *ab initio* calculations that show no ICS distortion[40], and the temperature dependences of the ICS and the CDW are very different (Supplementary Fig. 11). The last alternative possibility we will mention is Peierls-type or correlation-driven charge order. The former typically requires an electron Fermi surface while the latter usually appears at much lower energy scales than the Hubbard bands[32]. Such behavior is inconsistent with the ICS observed in our system and has no reasonable connection to the new periodicities seen here (i.e., $\mathbf{q}_{ICS}$ and $\mathbf{q}_{M}$).

The presence of a QSL-based spinon Fermi surface, on the other hand, very naturally explains both the energy-dependence and wavevectors of the $\mathbf{q}_{ICS}$ and $\mathbf{q}_{M}$ super-modulations that we observe in SL 1T-$TaSe_2$. The starting point here is that our system hosts a QSL state with a half-filled spinon band. This idea is supported by density matrix renormalization group

(DMRG) calculations based on the triangular-lattice *t-J* model with a ring exchange term that simulates the Hubbard model near a Mott transition[16]. In these calculations the spin-correlation peaks in the Γ-M directions are missing[16] which suggests that a partial gap opens at the spinon Fermi wavevector k_F along the Γ-M directions due to a Fermi surface instability (the calculations, however, don't reveal the precise source of the instability - Fig. 5a). The value of the predicted spinon k_F comes from the spinon band structure which is modeled using a zero-flux mean-field tight-binding Hamiltonian[10] with nearest-neighbor spinon hopping. This yields a value of the spinon Fermi wavevector in the Γ-M direction of $k_F \approx$ 0.375 reciprocal lattice units (r.l.u.) (inclusion of next-nearest-neighbor hopping does not significantly alter k_F – see Supplementary Note 3.2 and Supplementary Fig. 14).

The predicted instability of the spinon Fermi surface implies the existence of primary order wavevectors $\mathbf{P}_i = (1 - 2k_F)\mathbf{b}_i \approx 0.249\mathbf{b}_i$ that couple the gapped spinon Fermi surface regions in an extended zone scheme as shown in Fig. 5 (see red arrows in Fig. 5a and red dots in Fig. 5b). The absence of experimental LDOS super-modulations at these predicted wavevectors (Fig. 5c, d), however, suggests that the spinon Fermi surface instability is not a spinon density wave. Other candidates for the spinon Fermi surface instability, such as a spinon pair density wave[13,41-43] or a spinon spin density wave, are more consistent with our experiment since they cannot be imaged directly by conventional STM because they reflect spatial modulations in either the spinon pair channel (in the case of spinon pair density wave) or the pure spin channel (in the case of spinon spin density wave). However, a *composite* spinon density wave that is observable by conventional STM can be induced at higher harmonics of the primary $\mathbf{P}_i$'s. This can be rationalized in a straightforward manner from either a scattering picture or a Landau formulation[44,45] (Supplementary Notes 3.3, 3.4, and Supplementary Fig. 15).

We find that although the primary $\mathbf{P}_i$'s do not coincide with our observed super-modulation wavevectors, their higher harmonics (labeled $\mathbf{Q}_i$ and $\mathbf{Q}_i'$ in Fig. 5b) match our experimental super-modulations quite well. For example, the theoretical harmonics $\mathbf{Q}_i = \mathbf{P}_i + \mathbf{P}_{i+1} \approx 0.249(\mathbf{b}_i + \mathbf{b}_{i+1})$ match our experimentally measured super-modulations at $\mathbf{q}_{\text{ICS}} = (0.241 \pm 0.009)(\mathbf{b}_i + \mathbf{b}_{i+1})$ (Fig. 5c), while the theoretical harmonics $\mathbf{Q}_i' = 2\mathbf{P}_i$ match our experimentally measured super-modulations at $\mathbf{q}_{\text{M}}$ (Fig. 5d). Our experimental observation of the predicted harmonics at both $\mathbf{Q}_i$ and $\mathbf{Q}_i'$ strongly suggests the existence of a hidden primary wavevector $\mathbf{P}_i$ and points to a spinon Fermi surface subject to instability at $\mathbf{P}_i$ in SL 1T-$TaSe_2$.

If we work backwards and compare our measured value of $\mathbf{q}_{\text{ICS}} = q_{\text{ICS}}(\mathbf{b}_1 + \mathbf{b}_2)$ to the theoretically predicted composite spinon density wave vectors $\mathbf{Q}_i = \mathbf{P}_i + \mathbf{P}_{i+1}$ using $\mathbf{P}_i = (1 - 2k_{\text{F}})\mathbf{b}_i$ then we find that the spinon Fermi wavevector can be written as $k_{\text{F}} = (1 - q_{\text{ICS}})/2$. This leads to an experimental value of $k_{\text{F}} = (0.380 \pm 0.005)$ r.l.u., in good agreement with the theoretically predicted value of $k_{\text{F}} = 0.375$ r.l.u. This value of k_{F} is also consistent with our ARPES data which shows enhanced intensity centered at Γ that greatly weakens for in-plane momenta beyond k_{F} (Supplementary Fig. 3). Our observed temperature dependence of the ICS feature is also consistent with this physical picture since it suggests a spinon Fermi surface instability transition at a temperature of $T \sim 60$ K (Supplementary Fig. 11).

While the periodicities of our experimental super-modulations are well-explained by the QSL-based spinon scenario described above, a remaining question is how an STM that works by injecting charged particles (i.e., electrons) into a material can observe particles that have no charge (i.e., spinons). The answer lies in the process of fractionalization, whereby strongly correlated electrons in a QSL are predicted to separate into spinons (which have spin and no charge) and chargons (which have charge and no spin). Due to constraints in the total occupation of spinons and chargons, modulation of the spinon density can induce a small density modulation of physical charge[14]. However, an even stronger effect occurs in the tunneling process since an electron injected into the QSL UHB (or removed from the LHB) will fractionalize into (or recombine from) a spinon and a chargon (see sketch in Fig. 4c and d). The tunneling probability thus depends on both the spinon wavefunction and the chargon wavefunction, and so the tunneling rate of an electron at a particular energy can be expressed as a convolution of spinons and chargons that sum to the right energy, as done previously to interpret ARPES data[30,46] (Supplementary Note 3.5). Spatially periodic spinon density due to modulations from a spinon Fermi surface instability should thus modulate quasiparticle tunnel rates at the Hubbard band energies[11-13,16] (Supplementary Note 3.5 and Supplementary Fig. 16). Our experimental observation of long-wavelength super-modulations confined to Hubbard band energies (Fig. 4a and b) supports this proposed mechanism whether the super-modulations are thought to arise from a composite order picture or from scattering of spinons (both of which are essentially equivalent as described in Supplementary Note 3.3 and 3.4).

Despite the agreement of our experimental results with the existence of a QSL spinon Fermi surface, some mysteries remain. For instance, the $\mathbf{P}_i$ vectors are also second harmonic wavevectors of themselves (Supplementary Fig. 15b), and so their absence in our experiment must be explained. One possible explanation is that this is a consequence of small structure factors at $\mathbf{P}_i$ (Supplementary Note 3.3). We note that the selective visibility of composite density waves at higher harmonics has also been observed in other materials[47] and might be affected by detailed defect and domain structure (Supplementary Fig. 12). Another open question is the origin of the experimental CS pattern at the K-point wavevectors. The CS pattern cannot be explained as a consequence of a spinon Fermi surface since K is not a harmonic of the $\mathbf{P}_i$ wavevectors. One possible explanation of the short-range CS is that our

QSL phase is close to an antiferromagnetic ordered phase in the phase diagram, thus causing the CS to arise from short-range antiferromagnetic[48] fluctuations that are expected to be commensurate with the K-points (Supplementary Note 4).

In conclusion, our STM measurements provide evidence that single-layer 1T-$TaSe_2$ is a QSL with a spinon Fermi surface. Our observation of the Kondo effect in 1T-$TaSe_2$/1H-$TaSe_2$ heterostructures implies that SL 1T-$TaSe_2$ exhibits a triangular spin lattice, and our STS maps of 1T-$TaSe_2$ super-modulations directly reveal the effects of a spinon Fermi surface instability in this material. Our experimentally determined value of the spinon Fermi wavevector, $k_F = 0.380 \pm 0.005$ r.l.u., closely matches the theoretically predicted value of k_F = 0.375 r.l.u and supports the existence of a gapless QSL ground state. SL 1T-$TaSe_2$ thus provides a new platform to further investigate QSL phenomena such as the response of 2D QSLs to magnetic scatterers[14,49,50] and electrostatic doping[6,7,43].

Acknowledgments

We thank Dung-Hai Lee, Joel E. Moore, and Michael Zaletel for helpful discussions.

Funding:

This research was supported by the VdW Heterostructure program (KCWF16) (STM/STS measurements) and the Advanced Light Source (sample growth and ARPES) funded by the Director, Office of Science, Office of Basic Energy Sciences, Materials Sciences and Engineering Division, of the US Department of Energy under Contract No. DE-AC02-05CH11231. Support was also provided by National Science Foundation award DMR-1807233 (surface treatment and topographic characterization) and DMR-1926004 (theoretical QPI analysis). The work at the Stanford Institute for Materials and Energy Sciences and Stanford University (ARPES measurements) was supported by the DOE Office of Basic Energy Sciences, Division of Material Science. The work at beamline 4-ID-D of the Advanced Photon Source, Argonne National Laboratory (X-ray absorption measurements) was supported by the DOE, Office of Science, Office of Basic Energy Sciences, under Contract No. DEAC02-06CH11357. P.A.L. acknowledges support by DOE Basic Energy Science award number DE-FG02-03ER46076 (theoretical QSL analysis). S. T. acknowledges the support by CPSF-CAS Joint Foundation for Excellent Postdoctoral Fellows. J.H. and C.H. acknowledge fellowship support from the NRF grant funded by the Korea government (MSIT) (No. 2021R1A2C1004266). H.-Z.T. acknowledges fellowship support from the Shenzhen Peacock Plan (Grant No. 827-000113, KQJSCX20170727100802505, KQTD2016053112042971).

Author Contributions:

W.R., Y.C., P.A.L., and M.F.C. initiated and conceived this project. W.R., Y.C., R.L., H.-Z.T., S.K., F.L., C.J., and A.A. carried out STM/STS measurements under the supervision of M.F.C. W.R., Y.C., F.W., P.A.L., and M.F.C. contributed to microscopy data analysis. S.T., J. H., and H.R. performed sample growth and ARPES measurements/analysis under the supervision of C.H., Z.-X.S., and S.-K.M. W.R., Y.C., R.L., and S.K. performed XMCD measurements with support from Y Choi. M.W. performed DFT+U calculations under the supervision of S.G.L. P.A.L. provided theoretical support. W.R., Y.C., and M.F.C. wrote the manuscript with the help from all authors. All authors contributed to the scientific discussion.

Competing interests:

The authors declare no competing interests.

Methods

Sample growth and ARPES measurements

Both sample growth and ARPES measurements were performed at the HERS endstation of Beamline 10.0.1, Advanced Light Source, Lawrence Berkeley National

Laboratory. Single-layer $TaSe_2$ films were grown on both BLG/6H-SiC(001) and HOPG substrates in an ultrahigh-vacuum (UHV) MBE chamber under similar growth conditions as described elsewhere[29]. The substrate temperature was set at 660 °C, much higher than that for the growth of pure 1H-$TaSe_2$, to allow a simultaneous growth of single-layer 1T-$TaSe_2$ and single-layer 1H-$TaSe_2$, as well as vertical heterostructures composed of a 1T layer on top of a 1H layer. After growth, the samples were transferred in-situ into the analysis chamber with a base pressure 3×10^{-11} Torr for ARPES measurements at 12 K. The photon energy was set at 50 eV with energy and angular resolution of 12 meV and 0.1°, respectively. The samples were then capped by Se capping layers with ~10 nm thickness for protection during transport through air to the UHV STM chamber.

STM/STS measurements

STM and STS measurements were performed in a low-temperature ultrahigh-vaccum STM system (CreaTec) at $T = 5$ K (unless specified otherwise). Prior to measurements, the samples were annealed in UHV at ~200 °C for 3 hours to remove the Se capping layers and then immediately transferred in-situ into the STM stage sitting at $T = 5$ K. Electrochemically etched tungsten tips were calibrated on a Au(111) surface before measurements. $\mathrm{d}I/\mathrm{d}V$ spectra were collected using standard lock-in techniques ($f = 401$ Hz). $\mathrm{d}I/\mathrm{d}V$ mapping was performed in constant-height mode (i.e., with the feedback loop open).

XMCD measurements

XMCD measurements were performed at beamline 4-ID-D, Advanced Photon Source, Argonne National Laboratory. Hard X-ray was used to probe Ta L_2 and L_3 edges at grazing incident angles to optimize the signal from single-layer 1T-$TaSe_2$ relative to background noise from the substrate. Absorption spectra were collected in fluorescence yield mode. SL 1T-$TaSe_2$/BLG samples were capped with Se layers during transport to the XMCD measurement chambers. The samples were mounted with the sample plane in the vertical direction. The X-ray beam size was adjusted to be 0.1 mm along the horizontal direction and 0.3 mm along the vertical direction.

Data availability:

The data presented in Figs. 1-5 are available with the paper. All other data that support the findings of this study are available from the corresponding authors upon reasonable request.

Code availability:

The codes used in this study are available from the corresponding author upon reasonable request.

References

1 Anderson, P. W. Resonating valence bonds: a new kind of insulator? *Mat. Res. Bull.* **8**, 153-160 (1973).

2 Lee, P. A. An End to the Drought of Quantum Spin Liquids. *Science* **321**, 1306-1307 (2008).

3 Balents, L. Spin liquids in frustrated magnets. *Nature* **464**, 199-208 (2010).

4 Zhou, Y., Kanoda, K. & Ng, T.-K. Quantum spin liquid states. *Rev. Mod. Phys.* **89**, 025003 (2017).

5 Wen, X.-G. Quantum orders and symmetric spin liquids. *Phys. Rev. B* **65**, 165113 (2002).

6 Anderson, P. W. The Resonating Valence Bond State in La_2CuO_4 and Superconductivity. *Science* **235**, 1196-1198 (1987).

7 Lee, P. A. From high temperature superconductivity to quantum spin liquid: progress in strong correlation physics. *Rep. Prog. Phys.* **71**, 012501 (2008).

8 Shimizu, Y., Miyagawa, K., Kanoda, K., Maesato, M. & Saito, G. Spin liquid state in an organic Mott insulator with a triangular lattice. *Phys. Rev. Lett.* **91**, 107001 (2003).

9 Yamashita, M. *et al.* Highly Mobile Gapless Excitations in a Two-Dimensional Candidate Quantum Spin Liquid. *Science* **328**, 1246-1248 (2010).

10 Shen, Y. *et al.* Evidence for a spinon Fermi surface in a triangular-lattice quantum-spin-liquid candidate. *Nature* **540**, 559-562 (2016).

11 Motrunich, O. I. Variational study of triangular lattice spin-1/2 model with ring exchanges and spin liquid state in $\kappa-(ET)_2Cu_2(CN)_3$. *Phys. Rev. B* **72**, 045105 (2005).

12 Lee, S. S. & Lee, P. A. U(1) gauge theory of the Hubbard model: spin liquid states and possible application to κ-(BEDT-TTF)$_2$Cu$_2$(CN)$_3$. *Phys. Rev. Lett.* **95**, 036403 (2005).

13 Lee, S. S., Lee, P. A. & Senthil, T. Amperean pairing instability in the U(1) spin liquid state with fermi surface and application to kappa-(BEDT-TTF)$_2$Cu$_2$(CN)$_3$. *Phys. Rev. Lett.* **98**, 067006 (2007).

14 Mross, D. F. & Senthil, T. Charge Friedel oscillations in a Mott insulator. *Phys. Rev. B* **84**, 041102(R) (2011).

15 Law, K. T. & Lee, P. A. 1T-TaS_2 as a quantum spin liquid. *Proc. Natl. Acad. Sci. U. S. A.* **114**, 6996-7000 (2017).

16 He, W. Y., Xu, X. Y., Chen, G., Law, K. T. & Lee, P. A. Spinon Fermi Surface in a Cluster Mott Insulator Model on a Triangular Lattice and Possible Application to 1T-TaS_2. *Phys. Rev. Lett.* **121**, 046401 (2018).

17 Klanjšek, M. *et al.* A high-temperature quantum spin liquid with polaron spins. *Nature Phys.* **13**, 1130-1134 (2017).

18 Kratochvilova, M. *et al.* The low-temperature highly correlated quantum phase in the charge-density-wave 1T-TaS_2 compound. *npj Quantum Materials* **2**, 42 (2017).

19 Ribak, A. *et al.* Gapless excitations in the ground state of 1T−TaS_2. *Phys. Rev. B* **96**, 195131 (2017).

20 Yu, Y. J. *et al.* Heat transport study of the spin liquid candidate 1T−TaS_2. *Phys. Rev. B* **96**, 081111(R) (2017).

21 Murayama, H. *et al.* Effect of quenched disorder on the quantum spin liquid state of the triangular-lattice antiferromagnet 1T-TaS_2. *Phys. Rev. Research* **2**, 013099 (2020).

22 Wilson, J. A., Di Salvo, F. J. & Mahajan, S. Charge-density waves and superlattices in the metallic layered transition metal dichalcogenides. *Adv. Phys.* **24**, 117-201 (1975).

23 Fazekas, P. & Tosatti, E. Electrical, structural and magnetic properties of pure and doped 1T-TaS_2. *Philos. Mag.* **39**, 229-244 (1979).

24 Qiao, S. *et al.* Mottness Collapse in 1T−$TaS_{2-x}Se_x$ Transition-Metal Dichalcogenide: An Interplay between Localized and Itinerant Orbitals. *Phys. Rev. X* **7**, 041054 (2017).

25 Ritschel, T. *et al.* Orbital textures and charge density waves in transition metal dichalcogenides. *Nature Phys.* **11**, 328-331 (2015).

26 Ma, L. *et al.* A metallic mosaic phase and the origin of Mott-insulating state in 1T-TaS_2. *Nat. Commun.* **7**, 10956 (2016).

27 Cho, D. *et al.* Nanoscale manipulation of the Mott insulating state coupled to charge order in 1T-TaS_2. *Nat. Commun.* **7**, 10453 (2016).

28 Nakata, Y. *et al.* Selective Fabrication of Mott-Insulating and Metallic Monolayer $TaSe_2$. *ACS Appl. Nano Mater.* **1**, 1456-1460 (2018).

29 Chen, Y. *et al.* Strong correlations and orbital texture in single-layer 1T-$TaSe_2$. *Nature Phys.* **16**, 218-224 (2020).

30 Kim, B. J. *et al.* Distinct spinon and holon dispersions in photoemission spectral functions from one-dimensional $SrCuO_2$. *Nature Phys.* **2**, 397-401 (2006).

31 Ryu, H. *et al.* Persistent Charge-Density-Wave Order in Single-Layer $TaSe_2$. *Nano Lett.* **18**, 689-694 (2018).

32 Cai, P. *et al.* Visualizing the evolution from the Mott insulator to a charge-ordered insulator in lightly doped cuprates. *Nature Phys.* **12**, 1047-1051 (2016).

33 Ruan, W. *et al.* Relationship between the parent charge transfer gap and maximum transition temperature in cuprates. *Science Bulletin* **61**, 1826-1832 (2016).

34 Battisti, I. *et al.* Universality of pseudogap and emergent order in lightly doped Mott insulators. *Nature Phys.* **13**, 21-25 (2017).

35 Ruan, W. *et al.* Visualization of the periodic modulation of Cooper pairing in a cuprate superconductor. *Nature Phys.* **14**, 1178-1182 (2018).

36 Hewson, A. C. *The Kondo Problem to Heavy Fermions*. (The Press Syndicate of the University of Cambridge, 1993).

37 Nagaoka, K., Jamneala, T., Grobis, M. & Crommie, M. F. Temperature dependence

of a single Kondo impurity. *Phys. Rev. Lett.* **88**, 077205 (2002).

38 Helmes, R. W., Costi, T. A. & Rosch, A. Kondo proximity effect: how does a metal penetrate into a Mott insulator? *Phys. Rev. Lett.* **101**, 066802 (2008).

39 Madhavan, V. V., Chen, W., Jamneala, T., Crommie, M. F. & Wingreen, N. S. Tunneling into a Single Magnetic Atom: Spectroscopic Evidence of the Kondo Resonance. *Science* **280**, 567-569 (1998).

40 Ge, Y. & Liu, A. Y. First-principles investigation of the charge-density-wave instability in 1T-$TaSe_2$. *Phys. Rev. B* **82**, 155133 (2010).

41 Galitski, V. & Kim, Y. B. Spin-triplet pairing instability of the spinon fermi surface in a U(1) spin liquid. *Phys. Rev. Lett.* **99**, 266403 (2007).

42 Grover, T., Trivedi, N., Senthil, T. & Lee, P. A. Weak Mott insulators on the triangular lattice: Possibility of a gapless nematic quantum spin liquid. *Phys. Rev. B* **81**, 245121 (2010).

43 Xu, X. Y., Law, K. T. & Lee, P. A. Pair Density Wave in the Doped t−J Model with Ring Exchange on a Triangular Lattice. *Phys. Rev. Lett.* **122**, 167001 (2019).

44 Agterberg, D. F. & Tsunetsugu, H. Dislocations and vortices in pair-density-wave superconductors. *Nature Phys.* **4**, 639-642 (2008).

45 Fradkin, E., Kivelson, S. A. & Tranquada, J. M. Colloquium: Theory of intertwined orders in high temperature superconductors. *Rev. Mod. Phys.* **87**, 457-482 (2015).

46 Tang, E., Fisher, M. P. A. & Lee, P. A. Low-energy behavior of spin-liquid electron spectral functions. *Phys. Rev. B* **87**, 045119 (2013).

47 Edkins, S. D. *et al.* Magnetic field-induced pair density wave state in the cuprate vortex halo. *Science* **364**, 976 (2019).

48 Huse, D. A. & Elser, V. V. Simple variational wave functions for two-dimensional Heisenberg spin-1/2 antiferromagnets. *Phys. Rev. Lett.* **60**, 2531-2534 (1988).

49 Ribeiro, P. & Lee, P. A. Magnetic impurity in a U(1) spin liquid with a spinon Fermi surface. *Phys. Rev. B* **83**, 235119 (2011).

50 Norman, M. R. & Micklitz, T. How to measure a spinon fermi surface. *Phys. Rev. Lett.* **102**, 067204 (2009).

Fig. 1. Structure of single-layer $TaSe_2$ and 1T/1H vertical heterostructures.

a, Side-view of the crystal structures of single-layer 1T- and 1H-$TaSe_2$ as well as a 1T/1H vertical heterostructure on BLG-terminated SiC(0001). **b**, STM topographic image shows single-layer 1T-$TaSe_2$, single-layer 1H-$TaSe_2$, and a 1T/1H vertical heterostructure on BLG/SiC(0001) (V_b = -1 V, I_t = 5 pA). The insets are close-up images of the single-layer 1T and 1H islands (scanned at V_b = -0.5 V, I_t = 30 pA, and V_b = 50 mV, I_t = 1.3 nA, respectively) (T = 5K). **c**, Schematic of the triangular spin lattice and star-of-David charge density wave pattern in 1T-$TaSe_2$. Each star consists of 13 Ta atoms and has a localized spin represented by a blue arrow at the star center. The wavefunction of the localized electrons is represented by gray shading.

Fig. 2. Kondo resonance observed in a 1T/1H $TaSe_2$ vertical heterostructure.

a, Local electronic structure measured at T = 5 K via dI/dV spectroscopy for single-layer 1H-$TaSe_2$ (green), single-layer 1T-$TaSe_2$ (red), and a 1T/1H $TaSe_2$ vertical heterostructure (blue) (1H: V_b = -1.5 V, I_t = 30 pA, V_{mod} = 50 mV; 1T: V_b = 1.5 V, I_t = 40 pA, V_{mod} = 20 mV; 1T/1H: V_b = -1.5 V, I_t = 30 pA, V_{mod} = 20 mV). The insets show higher resolution dI/dV spectra (1H: V_b = 0.1 V, I_t = 30 pA, V_{mod} = 5 mV; 1T: V_b = -0.25 V, I_t = 30 pA, V_{mod} = 2 mV; 1T/1H: V_b = -0.1 V, I_t = 30 pA, V_{mod} = 1mV) (the Kondo peak in the inset is sharper and taller compared to the lower resolution measurement due to the use of a smaller wiggle voltage). **b**, Temperature dependence of the Kondo resonance peak observed in 1T/1H $TaSe_2$ vertical heterostructures for 5 K $\leqslant T \leqslant$ 70 K. The spectra are vertically offset for clarity (V_b = -0.1 V, I_t = 30 pA, V_{mod} = 1 mV). **c**, Temperature dependence of the intrinsic Kondo resonance width Γ (black with error bar). The error is estimated by the Γ threshold beyond which the fit significantly worsens[37]. The fit of Eq. (1) to the data (red dashed line) yields a Kondo temperature of T_K = 57 K.

Fig. 3. Super-modulations in single-layer 1T-$TaSe_2$ visualized by spectroscopic imaging. **a**, Large-scale topographic image of a single-layer 1T-$TaSe_2$ island (V_b = -1 V, I_t = 2 pA). **b**, The dI/dV spectrum of single-layer 1T-$TaSe_2$ (V_b = 1.5 V, I_t = 40 pA, V_{mod} = 20 mV). **c-g**, Constant-height dI/dV maps at different energies acquired in the area indicated by yellow dashed square in **a** (I_t = 30 pA, V_{mod} = 20 mV). **h-l**, Corresponding Fourier transforms (FTs) of the dI/dV maps in **c-g**. FT peaks circled in red reflect the primary reciprocal lattice vectors of the star-of-David CDW and the red hexagon represents the CDW Brillouin zone. FT peaks circled in blue (**i-k**) reflect the incommensurate super-modulation (ICS) at 0.62 V, 0.2 V, and -0.18 V. FT peaks circled in green (**k**) reflect the commensurate super-modulation (CS) (T = 5 K).

Fig. 4. Energy dependence of super-modulations in single-layer 1T-$TaSe_2$. **a**, Plot of Fourier transform (FT) amplitude as a function of both the wavevector $\mathbf{q} = q(\mathbf{b}_1 + \mathbf{b}_2)$ (q measured in units of $|\mathbf{b}_1 + \mathbf{b}_2| = 4\pi/a$) along the Γ-K direction (y-axis, indicated by black dashed line in the inset) and the sample bias voltage (x-axis). High FT amplitude (dark color) appears at $\mathbf{b}_1$+$\mathbf{b}_2$ (black dashed ovals), the ICS wavevector (blue dashed ovals), and the CS wavevector (green dashed oval) (T = 5 K). **b**, Energy dependence of the ICS strength (blue dots) shows enhanced amplitude at Hubbard band energies. The ICS strength is defined as the FT amplitude at the ICS wavevector ($\rho(E, \mathbf{q}_{ICS})$) divided by the FT amplitude at $\mathbf{q} = \mathbf{0}$ ($\rho(E, \mathbf{q} = \mathbf{0})$). The reference d$I$/d$V$ spectrum is plotted in black (T = 5 K). **c**, Schematic density of states of a Mott insulator. **d**, Cartoon of a tip-QSL tunnel junction. An electron injected into the strongly-correlated UHB of the QSL decays into a spinon and a chargon.

Fig. 5. Super-modulation periodicities predicted from spinon Fermi surface compared with experiment.

a, Schematic of spinon Fermi surface at half-filling (red) with partial gaps opening along the Γ-M directions. The black hexagon is the star-of-David CDW Brillouin zone and the black arrows ($\mathbf{b}_i$) are the primary reciprocal lattice vectors of the CDW Brillouin zone ($1 \leqslant i \leqslant 6$, only $\mathbf{b}_1$ and $\mathbf{b}_2$ are labeled). The spinon Fermi surface instability wavevectors $\mathbf{P}_i$ (red arrow) connect the partial gaps on different spinon Fermi surfaces in an extended zone scheme. **b**, Spinon Fermi surface instability wavevectors $\mathbf{P}_i$ (red dots) and harmonics $\mathbf{Q}_\mathrm{i}$ (blue dots) and $\mathbf{Q'}_\mathrm{i}$ (purple dots) in the CDW Brillouin zone. **c**, Fourier transform (FT) of the STM image of 1T-$TaSe_2$/BLG at V_b = 0.5 V (STM image shown in Supplementary Fig. 7a inset). Experimental ICS wavevectors $\mathbf{q}_\mathrm{ICS}$ are circled in blue (T = 5 K). **d**, FT of the STM image of 1T-$TaSe_2$/HOPG at V_b = -0.15 V (STM image shown in Supplementary Fig. 12j). Experimental super-modulation wavevectors $\mathbf{q}_\mathrm{M}$ close to the M points are circled in purple (T = 5 K).

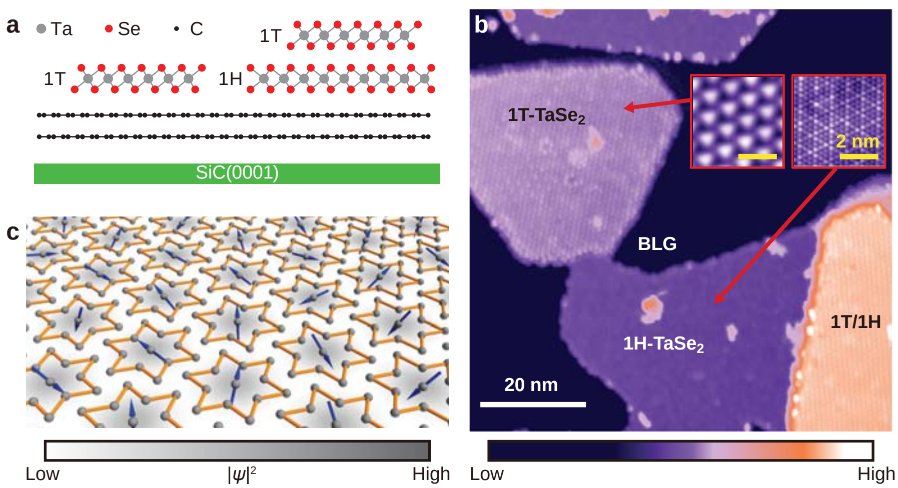

a
Ta
Se
C
1T
1T
1H
SiC(0001)
b
1T-TaSe2
2 nm
BLG
1H-TaSe2
1T/1H
20 nm
Low
High
c
Low
|ψ|2
High

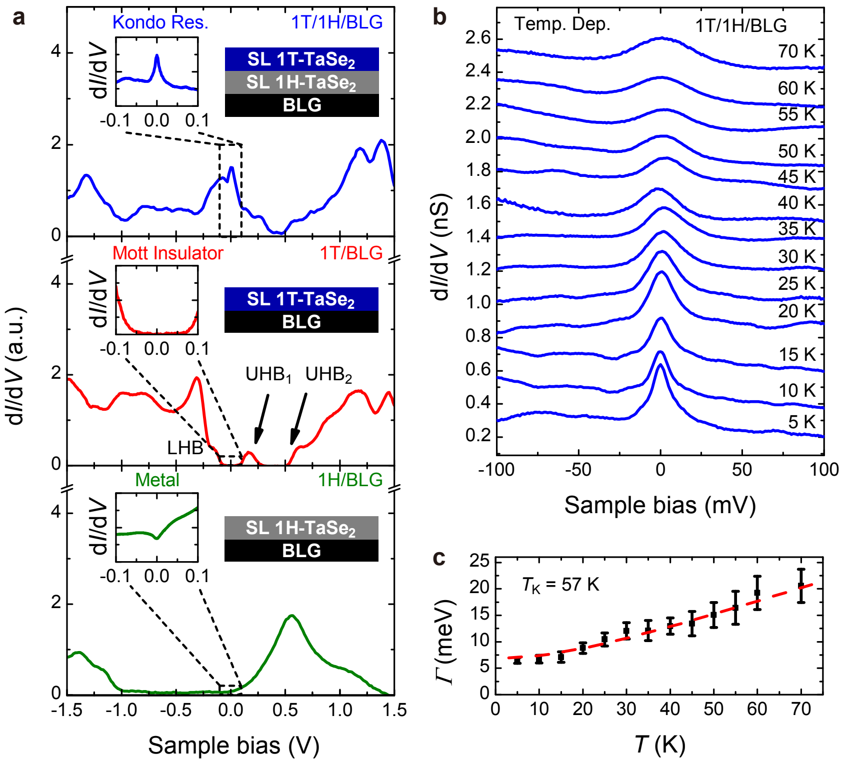
a
Kondo Res.
1T/1H/BLG
SL 1T-TaSe2
SL 1H-TaSe2
BLG
Mott Insulator
1T/BLG
UHB1
UHB2
LHB
Metal
1H/BLG
dI/dV (a.u.)
Sample bias (V)
b
Temp. Dep.
70 K
60 K
55 K
50 K
45 K
40 K
35 K
30 K
25 K
20 K
15 K
10 K
5 K
dI/dV (nS)
Sample bias (mV)
c
TK = 57 K
Γ (meV)
T (K)

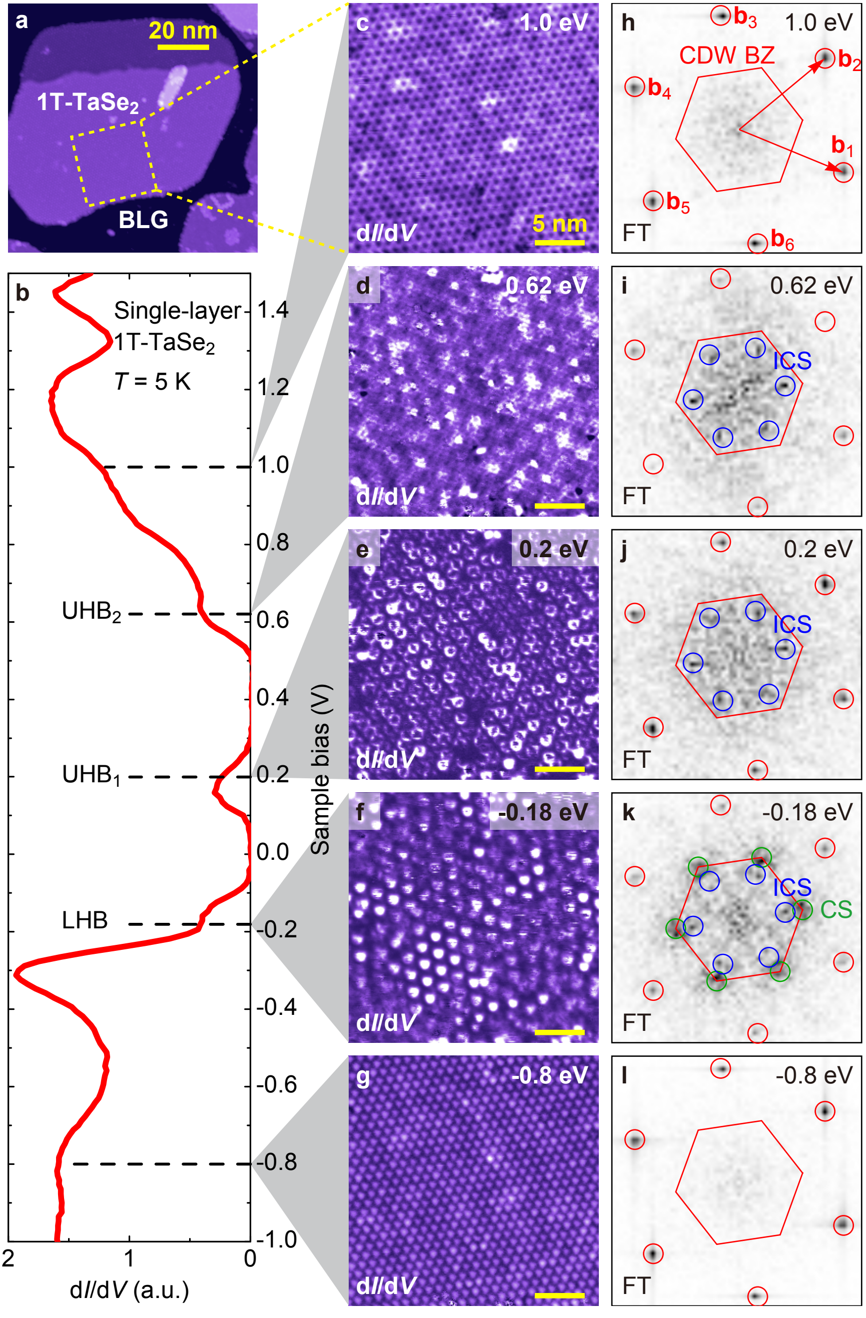

a
20 nm
1T-TaSe2
BLG
b
Single-layer 1T-TaSe2
T = 5 K
UHB2
UHB1
LHB
Sample bias (V)
dI/dV (a.u.)
c 1.0 eV
5 nm
dI/dV
d 0.62 eV
e 0.2 eV
f -0.18 eV
g -0.8 eV
h 1.0 eV
CDW BZ
b1
b2
b3
b4
b5
b6
FT
i 0.62 eV
ICS
j 0.2 eV
k -0.18 eV
CS
l -0.8 eV

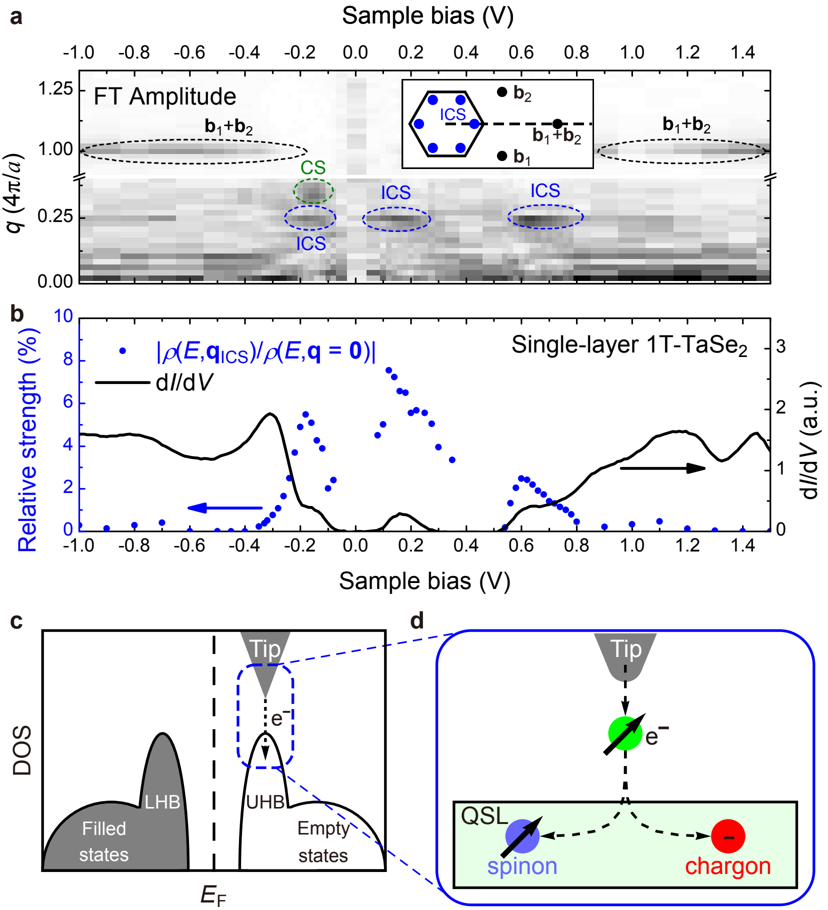
a
Sample bias (V)
FT Amplitude
b1+b2
CS
ICS
b2
b1
q (4π/a)
b
Relative strength (%)
|ρ(E,qICS)/ρ(E,q = 0)|
dI/dV
Single-layer 1T-TaSe2
dI/dV (a.u.)
Sample bias (V)
c
Tip
e−
DOS
LHB
UHB
Filled states
Empty states
EF
d
Tip
e−
QSL
spinon
chargon

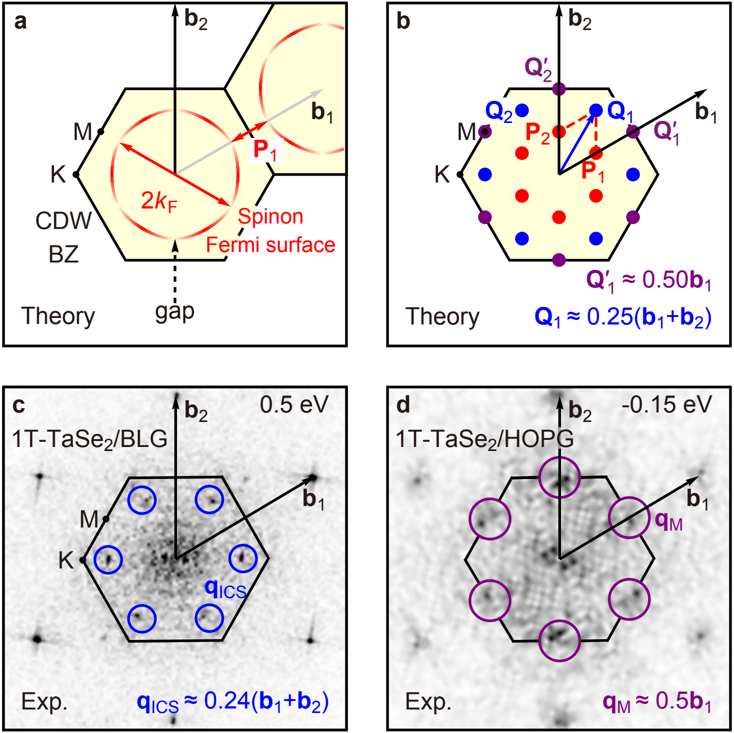
a
$\mathbf{b}_2$
$\mathbf{b}_1$
M
K
$\mathbf{P}_1$
$2k_F$
Spinon
Fermi surface
CDW
BZ
gap
Theory
b
$\mathbf{b}_2$
$\mathbf{Q}'_2$
$\mathbf{Q}_2$
$\mathbf{Q}_1$
$\mathbf{b}_1$
M
$\mathbf{P}_2$
$\mathbf{Q}'_1$
K
$\mathbf{P}_1$
$\mathbf{Q}'_1 \approx 0.50\mathbf{b}_1$
Theory
$\mathbf{Q}_1 \approx 0.25(\mathbf{b}_1+\mathbf{b}_2)$
c
$\mathbf{b}_2$
0.5 eV
1T-TaSe$_2$/BLG
$\mathbf{b}_1$
M
K
$\mathbf{q}_{ICS}$
Exp.
$\mathbf{q}_{ICS} \approx 0.24(\mathbf{b}_1+\mathbf{b}_2)$
d
$\mathbf{b}_2$
-0.15 eV
1T-TaSe$_2$/HOPG
$\mathbf{b}_1$
$\mathbf{q}_M$
Exp.
$\mathbf{q}_M \approx 0.5\mathbf{b}_1$